



Laser-Welded and Inflated Cold Plates for Battery Electric Vehicles: A Novel Approach

A study of laser-welded and gas hydroforming/inflated aluminum alloy cold plates was developed and applied to an AA3105-H24 prototype coupon

BY A. BOBEL, M. POUR, N. AVEDISSIAN, F. OKIGAMI, AND J. DELBOY

Abstract

Laser welding coupled with gas hydroforming is a novel approach for fabricating electric battery pack cooling plates. Obtaining continuous welds that can sustain inflation and pressurization tests is crucial. There are several challenges to achieving this, such as weld distortion, inflation spring back, and weld defects. Finite Element Analysis (FEA) is an appropriate and useful approach to predicting such behavior and anticipating any issues with prototype designs. In this study, the thermal-mechanical FEA modeling of laser welding and gas hydroforming of two AA3105 aluminum alloy sheets was done to study and validate the behavior of the assembly by comparing simulation results to 3D scans of welded and inflated parts. The simulation accurately reflected the global distortions measured postwelding and postinflation, with an overall decrease in global distortion observed and predicted after inflation. In addition, channel height spring back was accurately captured and compared to 3D light scan data.

Keywords

- Cold Plate
- Laser Welding
- Hydroforming
- FEA Modeling

Introduction

Battery electric vehicles (BEVs) require active cooling of the batteries, whether in the form of a cylindrical, pouch, or

prismatic can, to maintain the operating temperature of the cells during charging and discharge. These cooling plates can take various forms, such as cooling ribbons, module-level plates, and pack-sized plates (Ref. 1) to accommodate the various battery shapes used in the vehicle battery pack. For instance, cooling ribbons are commonly used in packs containing cylindrical cells, as they can weave between the closely packed cylinders and provide cooling to the cylindrical wall of the cell. Module and pack-sized plates typically provide cooling to one face or edge of the battery cells (i.e., pouch or prismatic) and require a thermal interface material (TIM) to fill gaps and voids between the cells and the cooling plate. Keeping the thickness of the TIM as uniform and thin as possible is key to achieving good thermal performance since the thermal conductivity of the TIM is significantly lower, only 1-5 W/mK (Ref. 2), than that of the cold plate itself. One critical factor in controlling TIM uniformity is the flatness of the cold plate.

Conventionally, module and pack-sized cold plates are made using controlled atmosphere brazing (CAB) of stamped aluminum alloy sheets (Ref. 3). The CAB process for aluminum is best characterized by closely controlled low-moisture and low-oxygen atmospheres with the use of fluxes for oxide removal to enable bonding at desired locations between components. However, continuous CAB furnaces can be capital intensive and have limitations on component size, and brazed parts have low mechanical properties after brazing. The loss in mechanical properties due to CAB processing is apparent in the commonly used cold plate AA3003 Al-Mn-based alloy, having an initial yield stress of 125 MPa pre-brazing and generally < 60 MPa yield stress post-brazing. When the cooling plate lies under the battery cells, the low strength of these alloys post-brazing necessitates the gauge to typically range between 1–2 mm to prevent yielding of the cooling channels during installation of the cells and wet out of the TIM. As such, manufacturing processes capable of utilizing higher-strength materials, compared to post-brazed AA3003, can enable lightweighting of the panels.

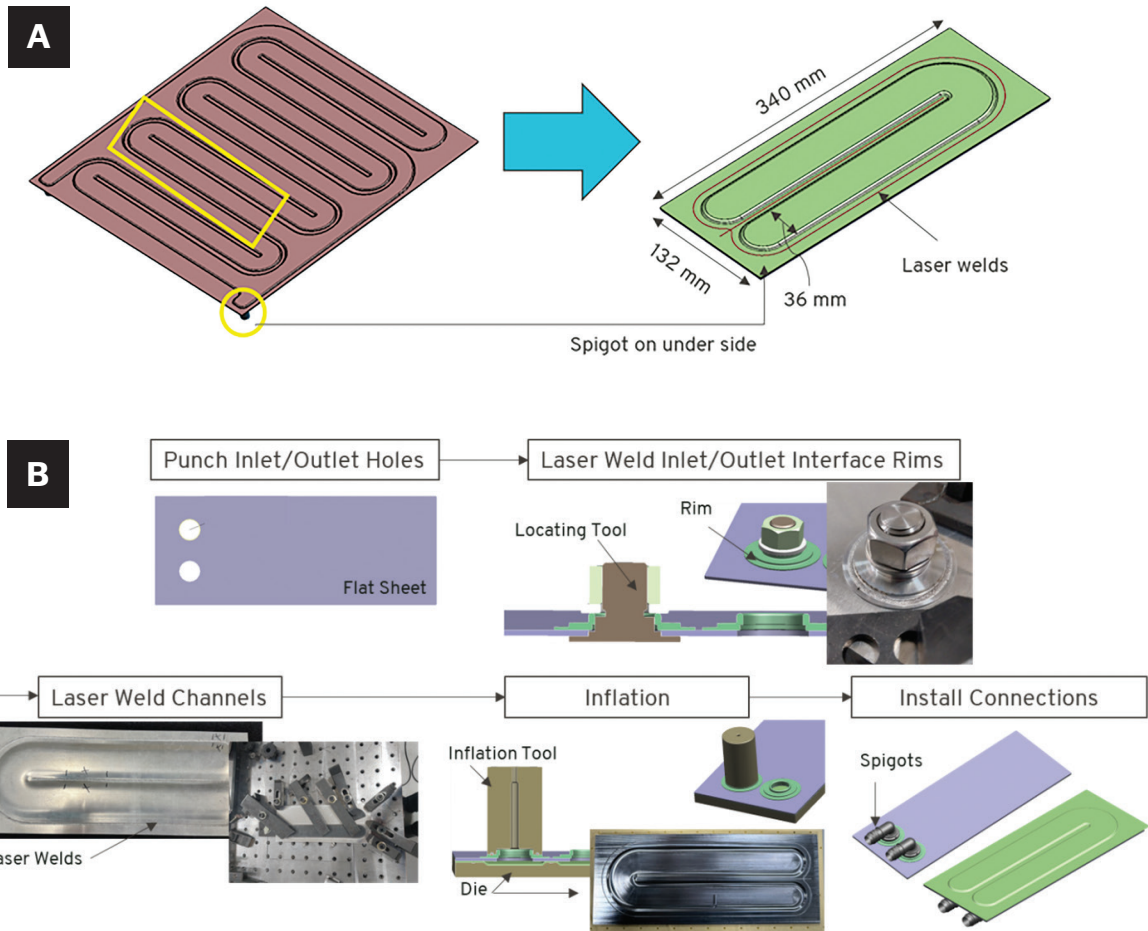


Fig. 1 – A – Coupon design with key features from a generic cold plate; B – manufacturing process for laser-welded and inflated battery cold plates.

Alternatively to CAB, laser welding and hydroforming are common manufacturing processes used for large-volume production of automotive components, including larger parts such as seat frames, space frames, and engine cradles, and those with higher strengths compared to the CAB process (Ref. 4). Combining the laser welding advantages of high-speed and noncontact with hydroforming's capability to make complex shapes presents a new manufacturing approach to produce cooling plates for BEVs. However, these processes present their challenges, including the formation of porosity during remote laser welding for gas-tight parts (Refs. 5–8), distortion from the heat input during welding (Refs. 9–11), forming limits during hydroforming (Refs. 12, 13), and spring back (Ref. 14).

Mitigation of porosity in laser welding of aluminum is essential in cold plates that must be hermetically sealed to prevent coolant leakage. In addition, the strength and durability of the weld must be sufficient to withstand both thermal and pressure cycle durability. Laser welding has been used in multiple e-mobility applications with advantages such as high welding speed, noncontact, and low energy input, resulting in narrow heat-affected zones and low thermal distortion. The reliability of the battery cold plate depends on the strength of laser welds between overlapped upper

and lower sheets. Poor weld quality in these connections can affect the mechanical performance and the potential for leaking. Compared to steel or copper alloys, aluminum alloys with a combination of relatively high thermal conductivity, low heat capacity, and low density are currently the most-favored material for battery cold plate applications. However, these advantages, along with low boiling elements, make aluminum laser welds more susceptible to porosity, particularly for the higher strength 6XXX series (Al-Mg-Si) and 7XXX series (Al-Zn) Al alloys.

Several methods have been investigated to address weld porosity by controlling the keyhole and melt pool geometry to minimize keyhole collapses, enlarge the melt pool size, and thus, suppress bubble formation. Li et al. (Ref. 15) achieved keyhole stability by defocusing the laser beam, thereby reducing the keyhole aspect ratio to suppress pore formation. An Adjustable Ring Mode (ARM) laser is a novel beam-shaping technique that combines two circular and donut-shaped laser beams at the focal point, which has shown advantages in keyhole stability and surface quality of welds (Refs. 16, 17) by enlarging the keyhole opening. Laser beam oscillation has also been demonstrated as an effective approach in reducing porosity. Fetzer et al. (Ref. 18) compared sinusoidal oscillation in both longitudinal and lateral directions with circular oscilla-

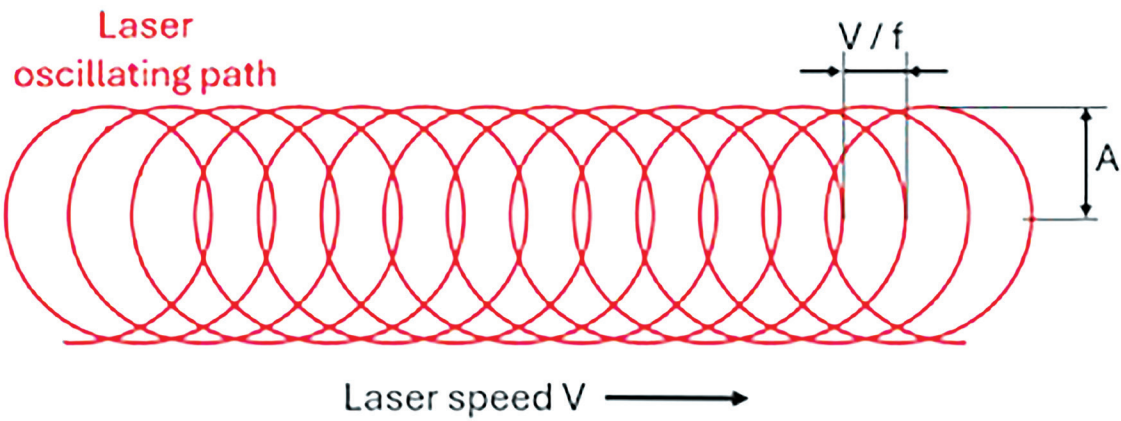


Fig. 2 – Schematic of oscillating laser welding for Al lap joints.

Table 1 – Nominal Chemical Composition (wt-%) of AA3105 as Per the Alloy Technical Data Sheet with Remainder as Al and Maximum Unless Shown as Range

Si	Fe	Cu	Mn	Mg
0.6	0.7	0.3	0.3–0.8	0.2–0.8
Cr	Zn	Ti	Others Each	Others Total
0.2	0.4	0.1	0.05	0.15

tion and found that circular oscillation was the most effective in eliminating pores by facilitating the reabsorption of bubbles by the keyhole during subsequent interactions. Li et al. (Ref. 19) and Ke et al. (Ref. 20) observed that beam oscillation reduced porosity by enlarging the melt pool, providing more time for bubbles to escape to the surface. Recent studies have also shown that the combination of ARM laser technology along with beam oscillation has effectively reduced the porosity in aluminum welds. Huang et al. (Ref. 21) showed that a circular oscillation ARM laser welding mode facilitates the reabsorption of bubbles by the keyhole, and stirring effects of the oscillation pattern create turbulence in the melt flow that prevents bubbles from reaching the solidification line. In this study, the combination of ARM laser and circular oscillation welding modes will be found to reduce porosity and improve weld quality with uniform penetration depth along the weld joint.

Hydroforming is traditionally utilized to manufacture sheet deep drawing and tubular components with complex shapes. Hydroforming brings the advantages of high forming limits, high precision, and fewer passes than traditional stamping processes. However, aluminum alloys with low formability can be challenging due to wrinkling and fracture when internal pressures are too high, particularly with complex shapes with multi-curved surfaces. BEV cold plates are relatively less complex, having very shallow channels, on the order of a couple of millimeters, making hydroforming an ideal forming technique.

Advancements in numerical simulation of laser welding and hydroforming have enabled the prediction and vir-

tual optimization of the manufacturing process. Different modeling approaches can be utilized in the welding phase. Computational fluid dynamics (CFD) and the finite element method (FEM) are the most-used numerical methods to model welding processes. Due to its high computational cost, CFD is routinely limited to local models that study melt pool dynamics, as shown by Allu (Ref. 22). The CFD model lacks the ability to predict mechanical results, such as stresses, strains, and distortions due to welding. For this reason, FEM will be used to model the laser welding process in this study. In laser welding FEM modeling, the heat input is approximated by a heat source geometry and the input power. Moraitis and Labeas (Ref. 23) presented some results for heat input and distortion from the laser beam welding (LBW) of two aluminum plates. Chen et al. (Ref. 24) studied the effect of preheating and unclamping time on the residual stress and distortion of LBW aluminum samples using the FEM.

Hydroforming modeling is restricted to either analytical or finite element models. The plastic deformation resulting from the internal pressure can be effectively modeled using distributed loads. Much literature is available on water hydroforming, but the method also applies to gas hydroforming. Ahmetoglu (Ref. 25) briefly reviewed hydroforming techniques, with experimental validation for different samples. Grizelj et al. (Ref. 26), presented some hydroforming shapes predicted by FEM models for high-strength steel sheet metal. Abedrabbo et al. (Ref. 27) discussed the wrinkling behavior in thin sheets of 6111-T4 aluminum with good correlation between experimental results and FEM models.

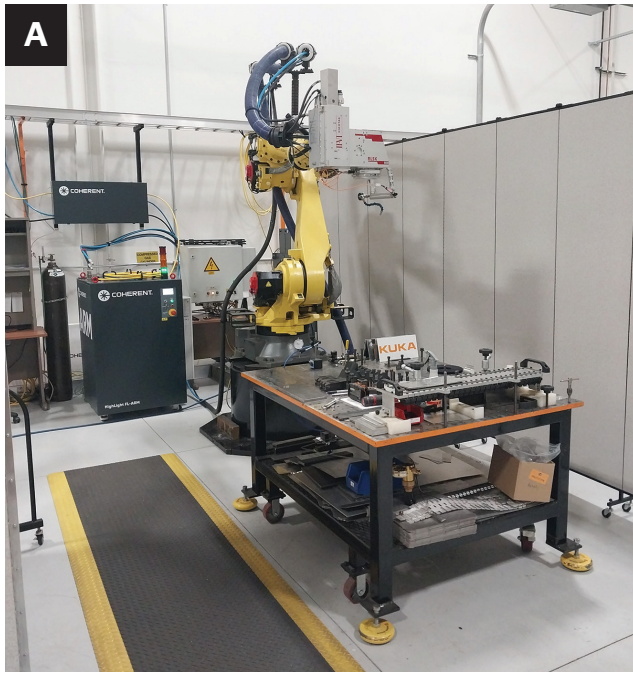


Fig. 3 – A – Laser welding setup; B – weld of interface rim; C – clamping strategy of center weld; D – representative clamping strategy of periphery welds.

Karabegović and Poljak (Ref. 28) explored the behavior of welded and hydroformed steel and aluminum samples and developed an analytical model to evaluate the influence of process variables on the experimental results. However, to the authors' knowledge, the literature for a combined numerical model of laser welding and hydroforming is still nonexistent.

This work combines the numerical modeling of laser welding and gas-hydroforming of a representative battery cold plate coupon with experimental validation. Two sheets of AA3105 Al were remote laser welded together to form a bonded blank that was then gas-hydroformed to inflate the cooling channel. A coupled thermomechanical FEM was calibrated to the laser heat input and utilized to simulate the temperature field and resultant distortion of the welded coupon before inflation and compared to 3D light scans of the physical coupon. Following welding simulations, subsequent numerical analyses of the gas-hydroforming process were performed on the welded blank, and the resultant inflated model predictions were compared to the physical coupon.

Experimental Procedure

A cold plate coupon was designed for this study, incorporating key features of a generic cold plate, including the spigots, straight channel lengths, and a channel turnaround. The coupon was approximately 340 mm long by 132 mm wide with 36 mm wide channels (Fig. 1A). The manufacturing process for cold plate coupons combining laser welding and

Table 2 – Characteristics of the Laser Beam Source, Delivery Optics, and Final Welding Parameters

Laser Source		Scanning Optics	
Model	Coherent ARM	Fiber Diameter	50/230 μm
Maximum Power	10 kW	Focusing Lens	450 mm
Wavelength	1070 nm	Collimating Lens	150 mm
Beam Quality	≤ 4 mm.mrad	Focus Diameter	150/690 μm
		Scan Field	200 mm X 300 mm

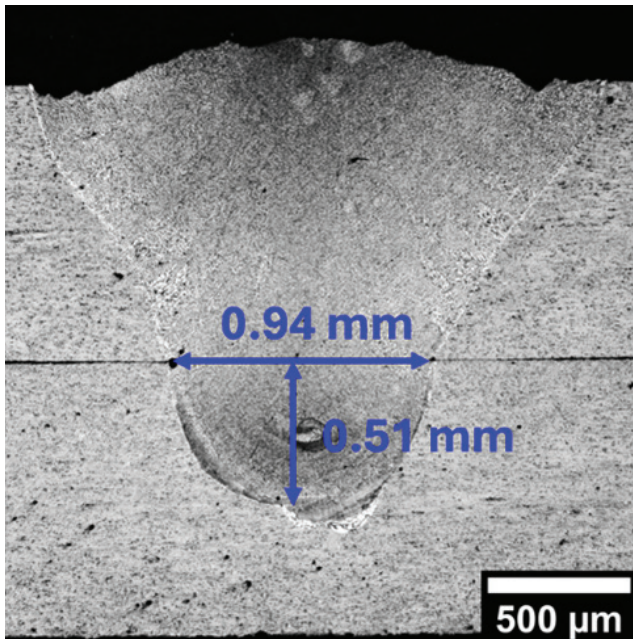


Fig. 4 – Weld cross section for test No. 7 condition as from Table 3.

gas-hydroforming is summarized in Fig. 1B. The first step involves cutting or punching of the inlet and outlet holes in the sheet that would become the flat side of the cold plate. The radius of the hole is nominally 12.68 mm. Only one of the two holes was made in this study, as no fluid flow testing was performed using this coupon geometry. After the hole is made, the interface rim is located and laser welded to the sheet. Subsequently, the channel laser welds are made using a series of three welds (to be discussed in more detail in the following section). After laser welding, the plate is placed onto a die with reliefs for the channels. An inflation tool is placed over the interface rim, and compressed gas (in this case argon) is introduced between the two welded sheets through the inflation tool and interface rim using 3.45 MPa (500 lb/in.²) of pressure. The sheet facing the die then yields and deforms to take the shape of the die. After inflation, the spigots are attached to the interface rim. The spigots for the coupons presented here were not attached to allow for better light scanning.

Material and Laser Welding

The aluminum alloy sheet utilized in this study was AA3105-H24 with a nominal composition as given in Table 1 and the following relevant mechanical properties: 139.9 MPa (0.02%) engineering yield stress (YS), 168.2 MPa engineering ultimate tensile stress (UTS), and total elongation of 9.5%. It is worth noting that the AA3105-H24 is significantly stronger than the 3003 post-braze properties typical of controlled atmosphere brazed cold plates with 51.1 MPa (0.2%) YS, 147 MPa UTS, and 17.5% elongation. This strength increase enables down gauging for lightweighting using the laser weld and gas-hydroforming process while still withstanding loads without yielding. In addition to the sheet, an interface rim made of machined AA3003 was used to represent a welded-on cooling plate inlet/outlet port. It was also used for the inflation gas-hydroforming process, which will be discussed later.

Welding experiments were carried out using a Coherent adjustable ring mode laser. This laser source emitted a total power of 10 kW continuous wave output power at $\lambda = 1070$ nm wavelength. The experimental set-up is illustrated in Fig. 3A. The laser beam was delivered from the laser source to the processing head scanning optic through an optical fiber with a core/ring diameter of 50 μm /23 μm . The collimation and focusing lenses with focal lengths of 150 mm and 450 mm resulted in a nominal beam diameter of 150 μm /690 μm on the focus plane. Table 2 summarizes the characteristics of the beam delivery system.

In an ARM laser, the core and ring beams can be adjusted separately, and it has been shown that the ring laser beam stabilizes the center laser-induced keyhole during the laser welding process (Ref. 29). Therefore, all experiments in this study used a constant laser power ratio (core/ring) of 0.7. The laser power and welding speed were kept constant, and the oscillation parameters were investigated to achieve the required weld geometry with low porosity. As schematically shown in Fig. 2, the oscillating amplitude (A) was the maximum deviation of the laser's oscillating path in the transverse direction, and the oscillating frequency (f) represented the number of circular patterns the laser completed every second. The parameters of the single variable testing method are presented in Table 3.

Welding was performed in an overlap configuration for both the interface rim and the sheets, with clamping of the joining partners being essential for a successful welding process. In all experiments, the laser beam focal plane was positioned on the surface of the top sheet. To have a stable clamping condition with no gap between the sheets, a fixture strategy was developed for welding purposes, as illustrated in Figs. 3B–D. Figure 3B shows the welding of the AA3003 interface rim with a 1 mm weld flange to one of the 1 mm gauge AA3105-H24 sheets, with a bolt through fixture used to locate the rim and provide additional clamping force. Figure 3C illustrates the clamping setup during the straight center weld, and Fig. 3D shows the first of the two periphery welds that closed off the channel formations.

Three samples were fabricated using the same welding parameters and configuration to evaluate process stability. Weld microstructure was evaluated using an optical microscope. Figure 4 depicts the representative cross section joint microstructure obtained from the weld coupon from test No. 7 in Table 3. Weld joints with a length of 100 mm were generated for process development, and cross sections were cut at three locations along the weld line at 30%, 50%, and 70% to minimize the effect of the start and end of the welding process. The hot-mounted transverse cross section of the welds was polished using grit sizes (200–1200) followed by polishing. Polished cross sections were etched with Keller reagent to better reveal the fusion zone boundaries. In this study, the criteria for selecting the welding parameters were interface width, penetration depth, and calculated average porosity across the representative cross sections of each test condition. The interface width, which represented the cross-sectional length of the weld interface at the faying surface, was targeted to be approximately 1 mm (100% of the thinnest material thickness). The penetration depth into the lower sheet was targeted to be approximately 0.5 mm (50% of the thinnest material thickness).

Gas-Hydroforming and 3D Light Scanning

Sheet gas-hydroforming was performed with an internal pressure configuration only. The welded blank was placed on a machined steel die, as shown in Fig. 5A, with the side having the interface rim fully clamped down except at the rim location. The plate was then “inflated” using compressed argon gas at 3.45 MPa (500 lb/in.²) and released from the die. Subsequently, the inflated sample was painted white using matte spray paint and 3D light scanned using a GOM ATOMOS SO 4M, as pictured in Fig. 5B.

3D scan analysis was performed in ZEISS Quality Suite INSPECT Optical 3D, as illustrated in Fig. 5C, for the uninflated and inflated samples. An initial axis alignment was performed using a 3-2-1 alignment, and erroneous nodes, such as those from the clamping fixture, were deleted. The two best-fit normal planes were constructed parallel to the face with the laser welds and the face with the interface rim. A surface comparison was then performed from the surface nodes of the scanned geometry to each of the two nominal planes previously generated for each face.

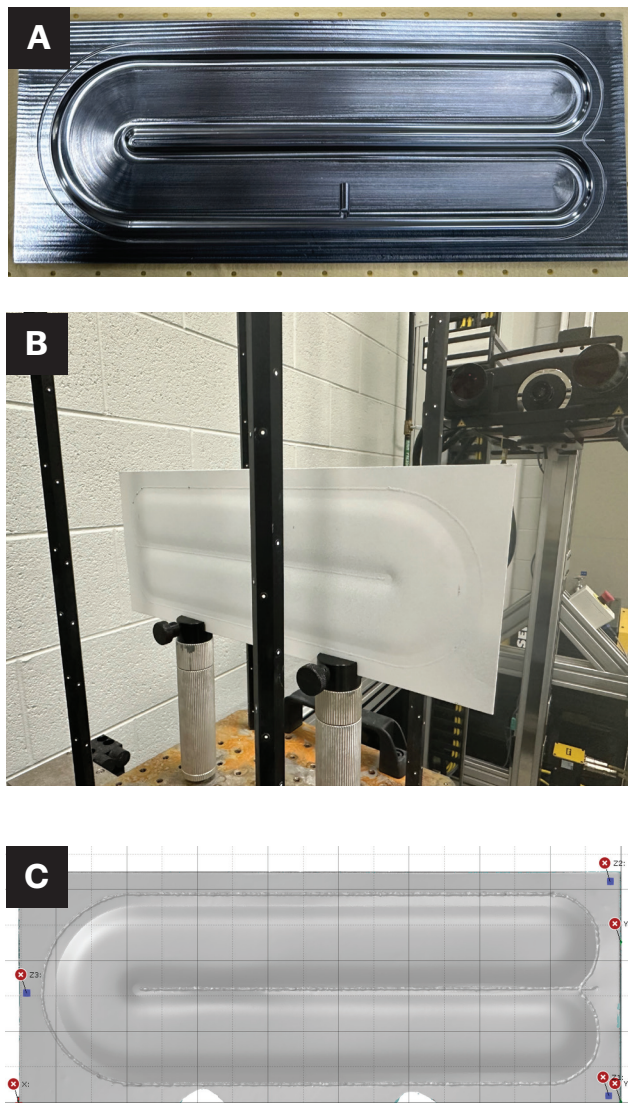


Fig. 5 – A – Gas-hydroforming inflation die with machined cavity for channel to inflate into; B – 3D light scanning setup and clamping arrangement; C – example of 3D light scan after axis alignment.

Numerical Model Development

The laser welding and hydroforming models were created in Hexagon’s Simufact Welding 2024.2 and Simufact Forming 2024.2, respectively. Both models consist of a fully coupled, thermal-mechanical, transient, nonlinear static finite element simulation (Ref. 30). The fixture and tooling are modeled as rigid bodies, and parts are modeled as deformable bodies with linear hexahedral elements.

Thermal boundary conditions included convection, governed by Equation 1, and a convective heat transfer coefficient (fixed at 20 W/m²K):

$$\frac{\dot{Q}_c}{A} = -h(T - T_0) \quad (1)$$

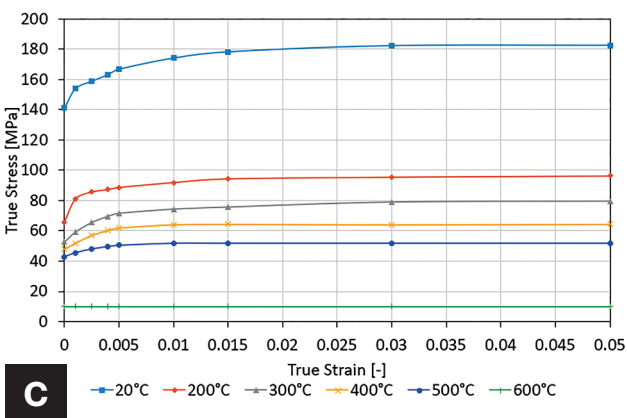
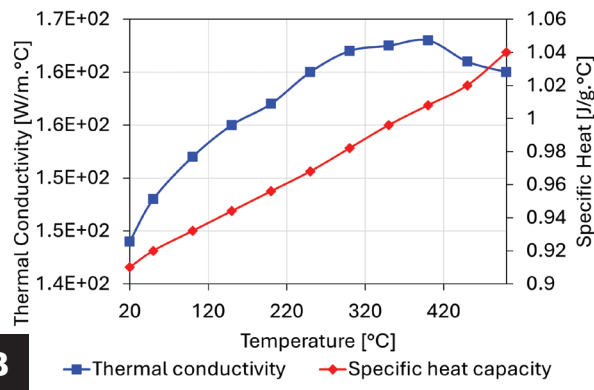
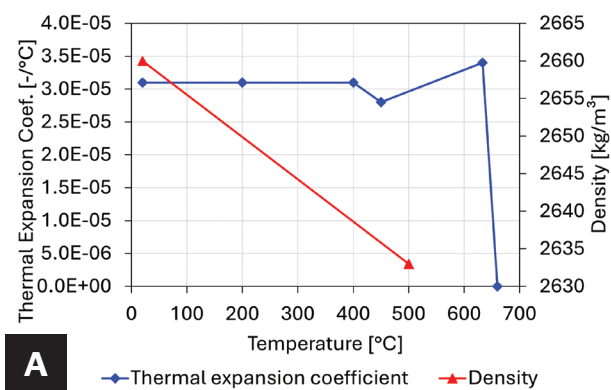


Fig. 6 – Temperature-dependent material properties used for simulation. A – Coefficient of thermal expansion (CTE) and density; B – thermal conductivity and specific heat capacity; C – true stress as a function of temperature.

where \dot{Q}_c is the convective heat loss, A is the surface area, h is the convective heat transfer coefficient, T is the instantaneous temperature, and T_o and the ambient temperature.

Radiation was considered in a simplified manner through an emission coefficient (fixed at 0.6), according to Equation 2:

$$\frac{\dot{Q}_r}{A} = -\varepsilon\sigma(T^4 - T_o^4) \quad (2)$$

where \dot{Q}_r is the radiative heat loss, A is the surface area, ε is the emission coefficient, σ is the Stefan-Boltzmann constant, T is the instantaneous temperature, and T_o is the ambient temperature.

Finally, conduction was controlled by the bulk material properties and by the contact heat transfer coefficient, which was fixed at 1000.0 W/m²K, according to Equation 3

$$\frac{\dot{Q}_b}{A} = -a(T_1 - T_2) \quad (3)$$

where \dot{Q}_b is the contact heat transfer, A is the contact area, a is the contact heat transfer coefficient, T_1 is the temperature on one side of the contact, and T_2 is the temperature on the other side.

The material model used temperature-dependent material properties, namely the thermal conductivity, specific heat, density, elastic modulus, and flow (stress-strain) curves, as summarized in Fig. 6. Room temperature mechanical property data were taken from tensile testing of the AA3105-H24 material. In contrast, temperature-dependent data were calculated using JMatPro[®] version 14.1 using the nominal chemical composition as listed in Table 1. The Poisson's coefficient was constant and equal to 0.3. The average chemical composition was used in cases with a range of compositions. The flow curves above room temperature were scaled according to the room temperature experimental tensile data.

Due to the cold work present in the material, local fusion due to welding would result in a local loss of strength. This effect was not considered in this case, since the focus of the study was on part deformation behavior and not on part strength and because the effect is more localized in laser welding when compared to other fusion welding processes such as arc welding. However, if a strength testing finite element analysis (FEA) model (such as burst testing) is to be done, this effect should be included, along with an appropriate damage model, so the local loss in mechanical strength and increased ductility are correctly captured.

Laser Weld Model

The laser weld model was divided into two sub-stages: the first for the rim weld and the second for the channel welds. The coupon design defined the laser track trajectories from the nominal weld locations. Figure 7 shows the model view for the rim (A) and channels (B) laser welding models, (C) the detail of the locally refined mesh, and (D) the detail of the heat source. The table is shown in blue, the two sheets and rim in grey, the clamps in red, and the laser track as a dotted red and yellow line. The total number of elements and nodes in the final model was 194,082 and 286,618, respectively.

The heat input was defined as a moving cylindrical volumetric heat source with 0.8 mm upper radius, 0.2 mm lower radius, and 1.7 mm depth. The power was defined as 2650 W and 2200 W for the rim and channel welds. The welding speed

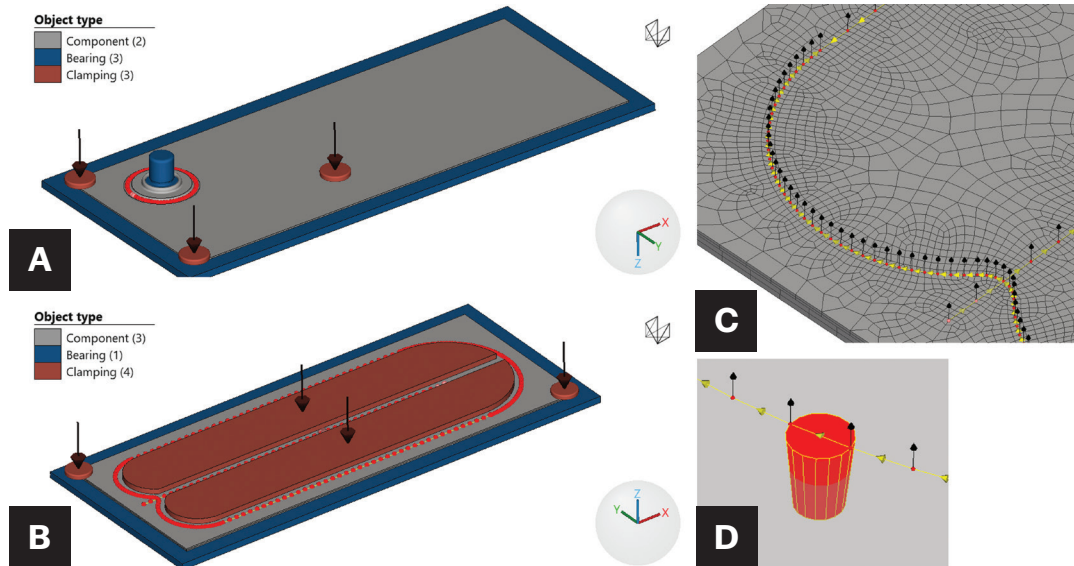


Fig. 7 – A – Model view for welding model of stage 1 (rim weld); B – model view for welding model of stage 2 (channel welds); C – detail of mesh refinement; D – detail of heat source.

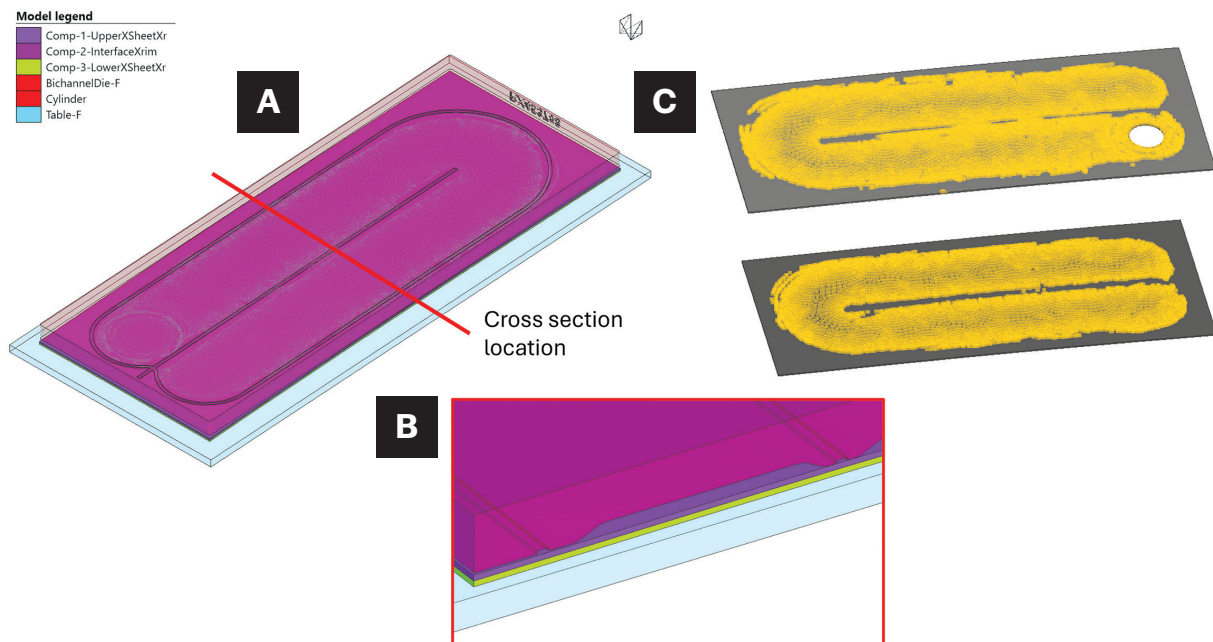


Fig. 8 – A – Model view of the hydroforming model; B – cross-section view; C – detail of the region with applied pressure in yellow.

was defined as 5 m/min. The efficiency value was calibrated to match the experimental fusion zone dimensions better. This is a common procedure for FEM welding modeling (Ref. 9) since the true efficiency is not easily measurable in the experiment. The final efficiency used was 67%. This value was calibrated for the channel welds cross section and transferred to be used in the rim weld model, since no detailed material information was readily available for the rim material. The results for the cross section of both welds are shown in the “Results and Discussion” section.

During welding of the interface rim, as shown in Fig. 7A, the sheet (grey) was held by three clamps (red) with a force of 100 N each. A table (blue) supported the sheet from below, and a pin/nut pair (locating tool as in Fig. 1B and Fig. 3B) was used to center the interface rim to the hole and clamp the rim to the sheet. In the channel welds stage (Fig. 7B), the two sheets were held by clamps that mimicked the real-life setup, as shown in Fig. 3C, D, with a force of 100 N each. A table supported both sheets from the bottom.

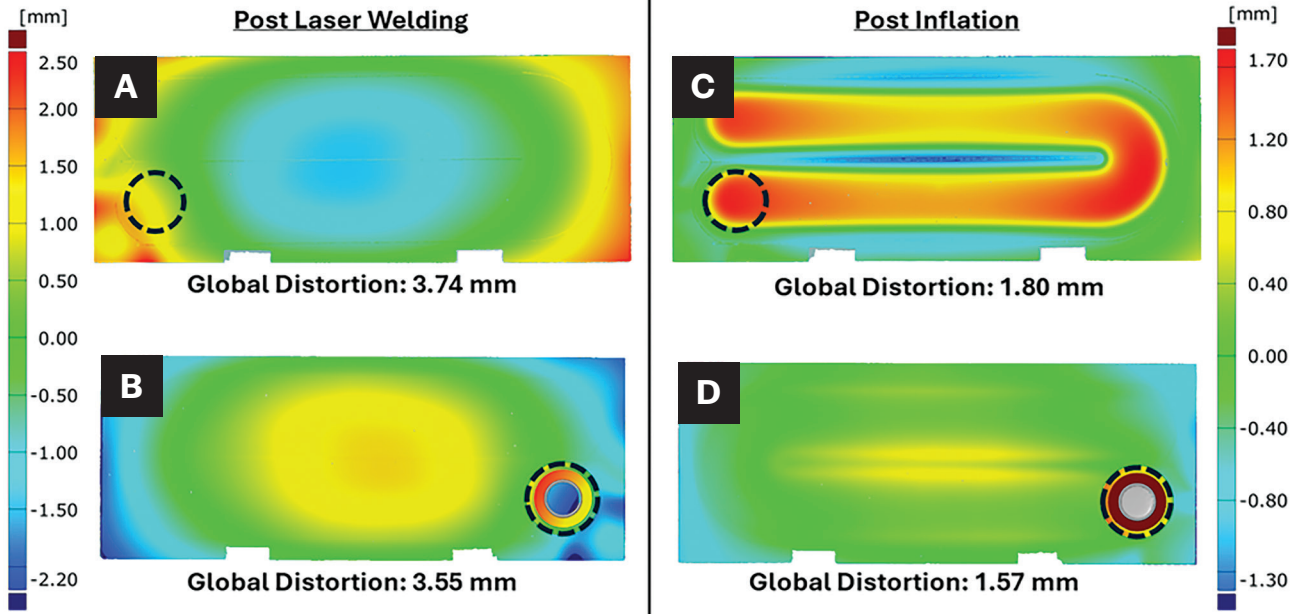


Fig. 9 – Light scans of the following: A – preinflation laser/channel weld side; B – preinflation rim side; C – postinflation laser/channel side; D – postinflation rim side.

Sliding contact was allowed between parts and between parts and boundary conditions. For the sheets, a “glued” (tied) contact was established between nodes if the melting point of the material was reached. This approach effectively represented the welding locations and only connected the regions that reached the melting point of the material. The remaining regions maintained a sliding contact behavior.

After welding, 60 s of cooling time was allowed, followed by the deactivation of the boundary conditions. The lower sheet was then held with fixed nodes near its center of gravity to allow free spring back of the parts. This was done after the rim welds and the channel welds. Before the channel welds stage, the clamps were moved to the “open” position to accommodate the spring back coming from the rim weld stage, and the sheets were clamped in place before welding. This was important since it realistically introduced clamping-related residual stresses into the assembly.

In the real process, the channel welds were divided into three different stages to allow clamping the parts while still maintaining a free path for the laser. The weld model was run with a multistage and a single- (combined) stage approach, and only minimal differences were observed. For this reason, the results for the single-stage approach are presented here. After welding, the clamping geometries were deactivated, and the geometry could freely spring back due to residual stresses and strains.

The welding model used a fixed time-stepping scheme for the welding portion. The time step was automatically calculated based on the welding speed. The cooling load case used temperature-based adaptive time stepping, which increased or decreased the time step size depending on the temperature changes between increments. The friction coefficient was defined as 0.2 for all contact pairs, and the contact type used was node-to-segment.

Hydroforming Model

The result files from the Simufact Welding model were loaded to Simufact Forming using a proprietary result format (ARC) for the hydroforming model. The quantities in the file included all major results, such as the stress tensor, strain tensor, displacement vector, peak temperatures, and instantaneous temperatures.

The result file contained the result for the last step of the welding simulation, where the part already presented significant distortion. Because of that, the inflation tooling started in the open position and was gradually closed to the inflation position (referred as clamping stage from hereon). The clamping stage was controlled by a time-dependent force application on one of the tools. To guarantee complete contact between the die faces and the sheets, a total force of 88 kN (20,000 lbs) was applied over a 0.5-s period. This force was necessary to resist the counterforces during the inflation step. Future studies will investigate the effect of clamping force on the sheets’ inflation and spring-back behavior.

After clamping, the internal pressure was modeled using a pressure boundary condition applied to the interior faces of the sheets (inside of the welded area). Figure 8 shows (A) the model view with the tooling and sheets in the open position, (B) a cross-section view of the geometries, and (C) the region on both sheets where pressure was applied. The region selection was done with a plane/angle-based algorithm and could not be executed precisely. Still, the selected region was deemed acceptable since it was constrained to the region inside the weld area. The total pressure applied was 3.45 MPa (500 lb/in.²), as used to manufacture the physical samples. The pressure ramped up in 0.5 s, was maintained for 0.5 s, then ramped down to zero over 0.5 s. After the pressure was removed, the tooling was deacti-

vated, and the sheets were held in place using fixed nodes near the center of gravity of one of the sheets. This was done to enable free spring-back of the geometries.

The inflation model used a fixed time stepping of 0.05 s and a hybrid contact algorithm. This algorithm combined aspects of the node-to-segment contact (usually faster) with the more precise contact patch calculation of segment-to-segment contact. The friction coefficient was defined as 0.2 for all contact pairs.

Results and Discussion

Laser Welding Parameter Selection

The resultant welding parameter selected for the AA3105-H24 1 mm-to-AA3105-H24 1 mm sheet weld was that of test No. 7 with a core/ring power of 900/1300 W, circular oscillation with 400 Hz, 0.3 mm oscillation amplitude, and speed of 5 m/min. For the AA3003 interface rim to AA3105-H24 1 mm sheet weld, only the power was increased to 1150 W and 1500 W, respectively, for the core and ring.

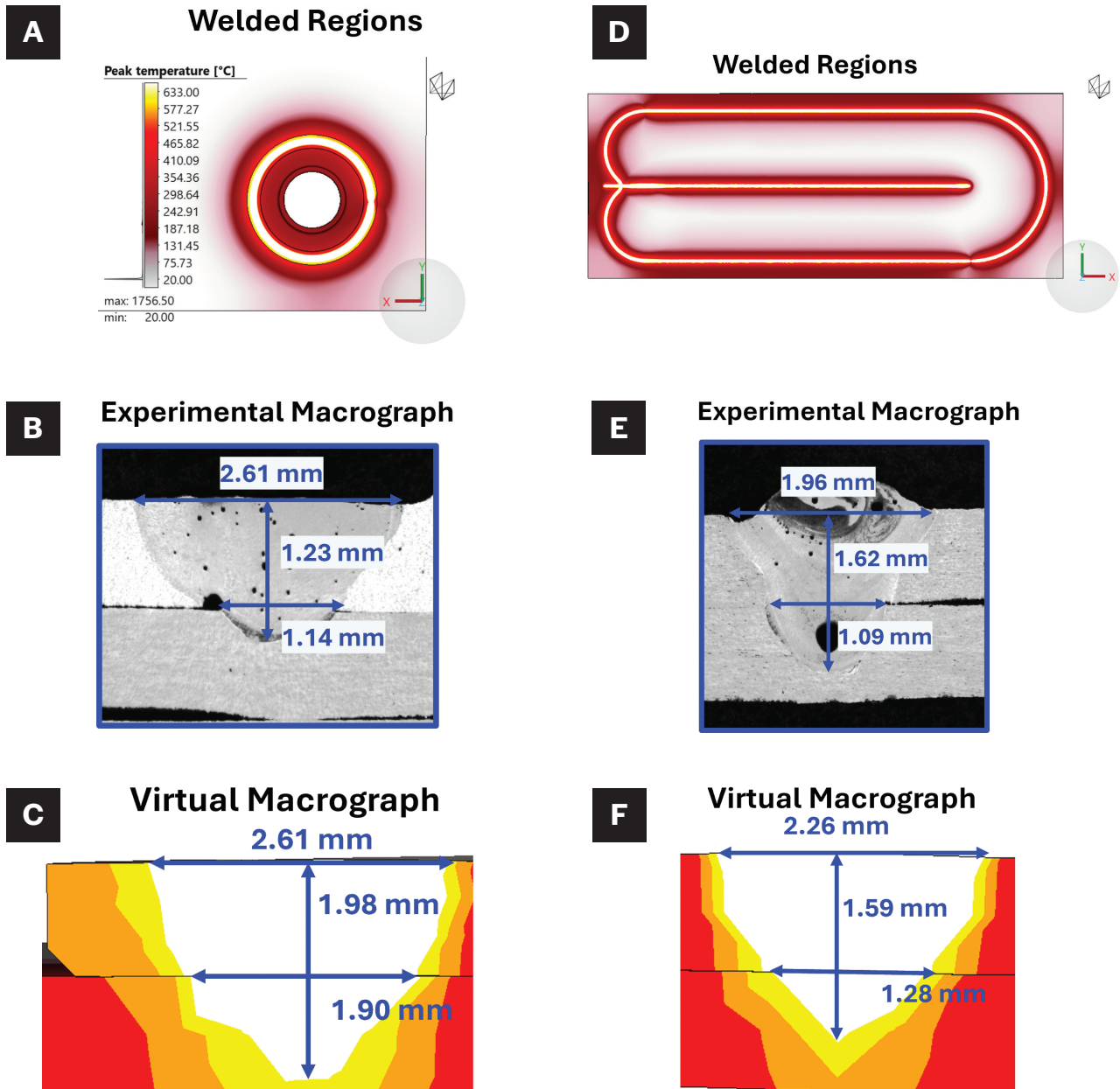


Fig. 10 – A – Interface rim peak temperature plot; B – rim experimental cross section; C – rim numerical cross section; D – channel welds peak temperature plot; E – channel weld experimental cross section; F – channel weld numerical cross section. Note: The temperature scale in A is the same as in C, D, and F.

3D Light Scan Results

The 3D light scans from the most distorted cold plate coupons in both the postwelding and postinflation states are shown in Figs. 9A, B, and C, D, respectively. The deviation from a nominal flat plane is shown for each side of the coupon. It was observed that post laser welding, the global distortion, measured as the difference between the middle region and

the corner regions, was between 3.55 and 3.74 mm. It is worth noting that coupon global distortion did vary post laser welding between coupons, with some coupons achieving global distortions as low as 1.88 mm. The corners were found to bow toward the laser-welded side of the coupon, with additional local distortion observed caused by the interface rim weld, the location of which is annotated by the black dashed line for reference. Following inflation, the global distortion

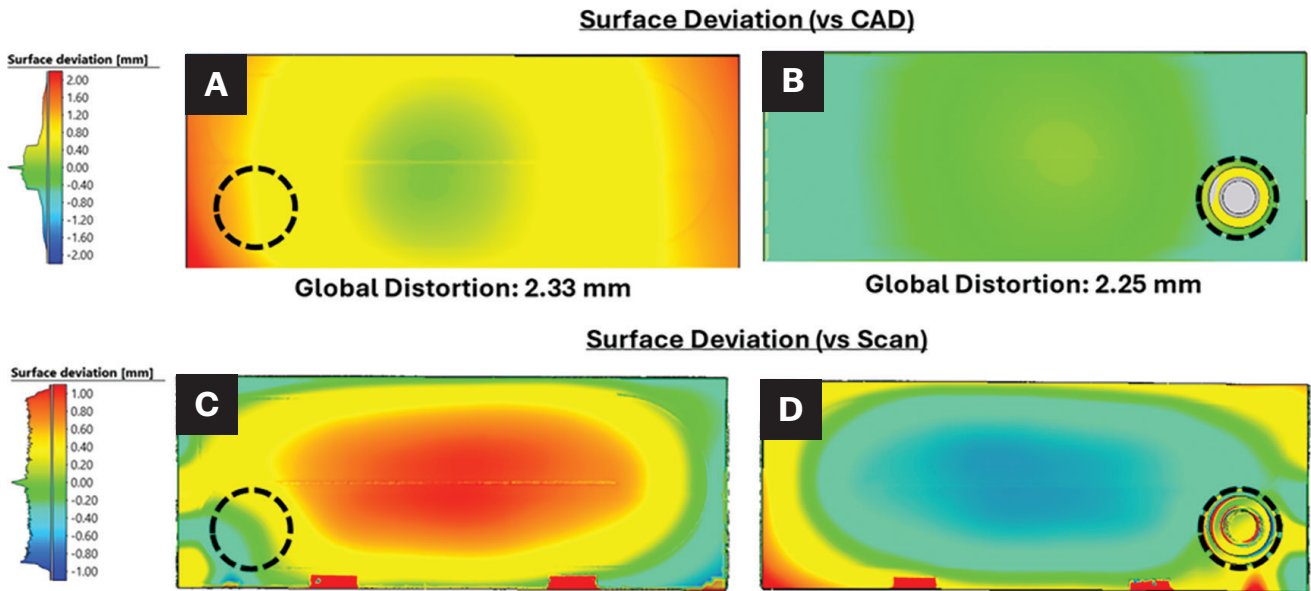


Fig. 11 – Surface deviations vs. CAD for postweld condition from the following: A – Laser side; B – interface rim side. Surface deviations vs. 3D light scan as from Fig. 9 for postweld condition from the following: C – laser side; D – interface rim side. The black dashed line corresponds to the general location of the interface rim.

Table 3 – Welding Process Parameters Explored for AA3105-H24 1 mm to AA3105-H24 1 mm

Test No.	Laser Power (W)		Welding Speed (m/min)	Oscillation Frequency (Hz)	Oscillation Amplitude (mm)
	Core	Ring			
1	900	1300	5	100	0.75
2	900	1300	5	100	1.5
3	900	1300	5	200	0.45
4	900	1300	5	200	0.9
5	900	1300	5	300	0.35
6	900	1300	5	300	0.7
7	900	1300	5	400	0.3
8	900	1300	5	400	0.6

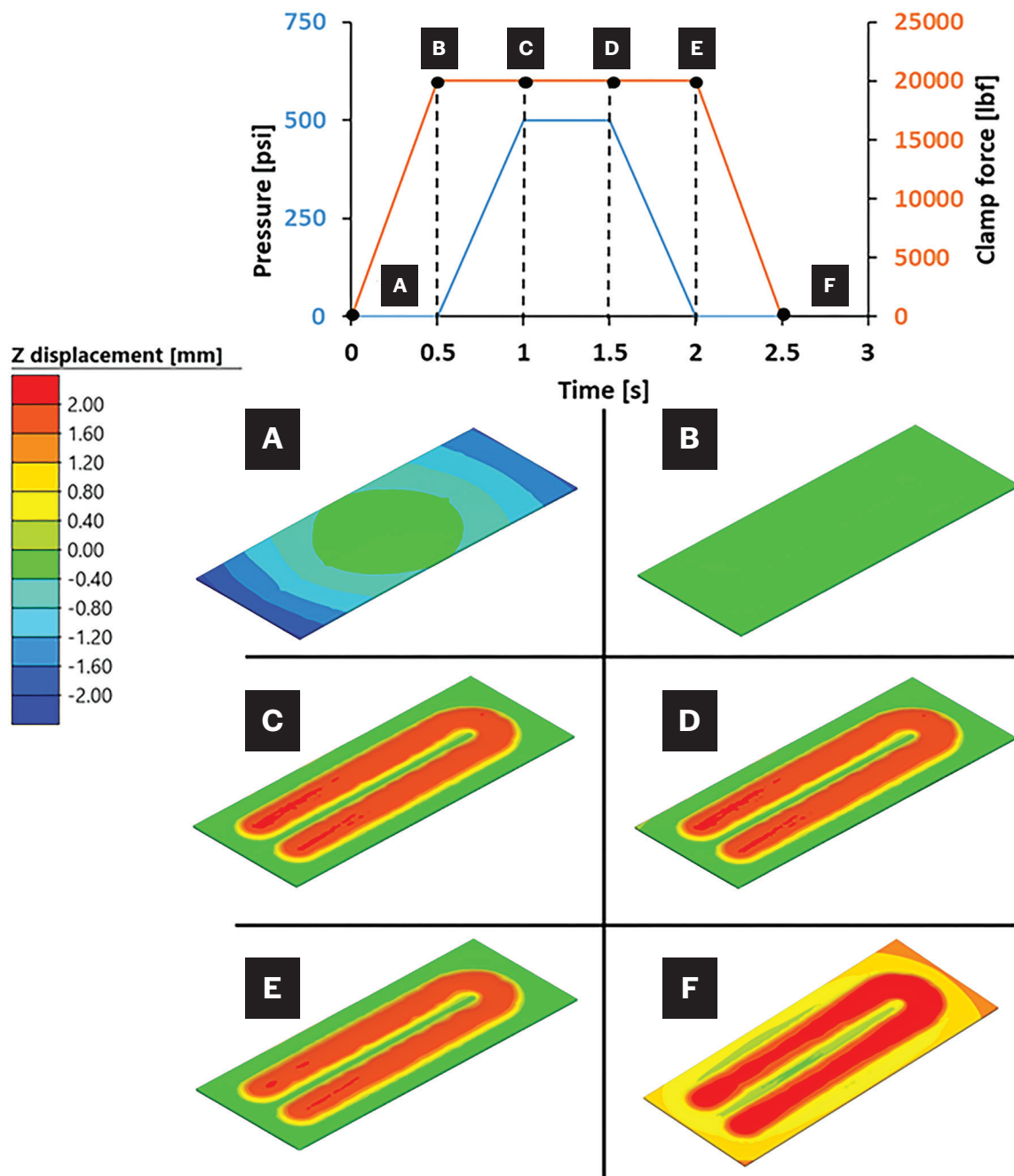


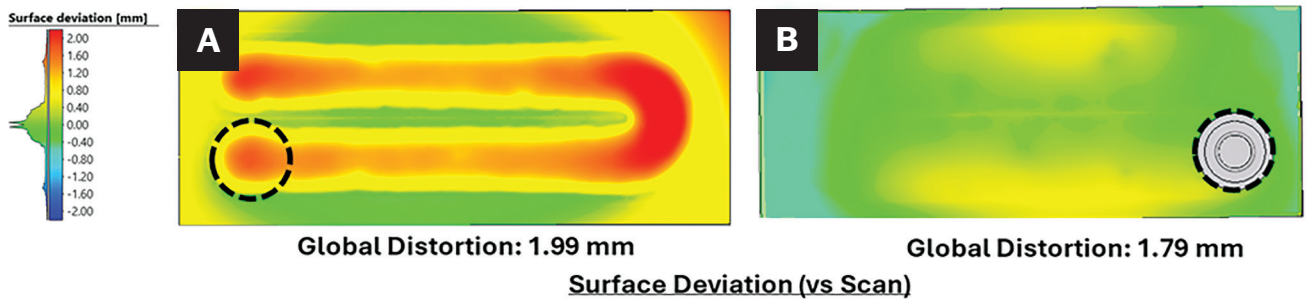
Fig. 12 – A – Pressure and clamping force evolution graph; B-F – vertical (Z) displacement evolution for inflated side.

in the coupon was found to decrease, ranging from 1.57 to 1.80 mm for the shown coupon. A slight bow remained along the length of the coupon. The channels were inflated with a relative height of about 1.52–1.85 mm, slightly below the nominal channel height of 2.0 mm machined into the die. These physical light scans formed the basis by which the laser weld and inflation model distortions will be compared.

Welding Model Results and Comparison

As previously mentioned, the simulated weld fusion zone was calibrated and compared to the experimental cross sections. Figure 10 shows the peak temperature plots highlighting all welded regions in the model (A) for the interface rim and (D) for the channels. Figure 10 also shows (B, E) the experimental cross section and (C, F) the virtual cross section for the interface rim weld and channel welds, respectively. The legend uses a white color for every region above the material's melting point, making it easy to compare the fusion zones.

Surface Deviation (vs Flat CAD)



Surface Deviation (vs Scan)

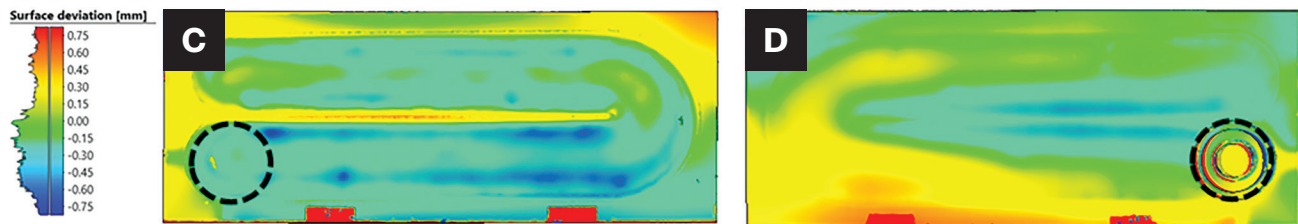


Fig. 13 – Surface deviations vs. Flat CAD for postinflation condition from the following: A – Laser side; B – interface rim side. Surface deviations vs. 3D light scan as from Fig. 9 for postinflation condition from the following: C – laser side; D – interface rim side. The black dashed line corresponds to the general location of the interface rim.

Comparing the fusion zones for the channel welds (Figs. 10E, F) to which the heat input model was initially calibrated, the heat input model resulted in a very accurate reproduction of the physical cross section. The penetration depth was within 0.03 mm, the upper face width was within 0.3 mm, and the width at the interface between the two sheets was within 0.19 mm. Similarly, comparing the fusion zones of the interface rim weld, which was based on the channel weld calibration but with increased power, the penetration depth was within 0.75 mm, the upper face width was the same as the experiment, and the interface between the two sheets was within 0.76 mm. As expected, the interface rim weld cross-section profile was less accurate with only power scaling considered. Further accuracy for the rim weld fusion zone can be obtained using a separate heat source calibration. Regarding the porosity observed in the experimental cross sections (Figs. 10B, E), the circular porosity was evidence of entrapped gas within the weld; however, this was deemed acceptable as hermetic sealing was maintained in the resultant welded parts.

The surface deviation for the laser welding model results as referenced to the flat CAD sheet is shown in Fig. 11A for the laser welded side and Fig. 11B for the interface rim side. The interface rim is annotated with a black dashed line. The same distortion trends were observed in the laser weld model results as in the physical samples, as shown in Fig. 9, with a bow forming toward the laser-welded face. The global distortion predicted by the laser weld model was 2.25–2.33 mm, within the variations of global distortions measured across multiple physical samples of 1.88–3.74 mm, as mentioned in the “Experimental Procedure” section. The comparison of the laser weld model prediction directly to the 3D light scan after best fit alignment is shown in Fig. 11C for the laser welded side and Fig. 11D for the interface rim side. The laser model simulated distortion was within approximately ± 1 mm of both sides of the welded coupon. It is worth noting that

while the laser weld model predicted some distortion during the interface rim weld step, it did not predict localized distortion around the interface rim following the channel welding. Additional studies on the interface rim weld and effects of the locating tool and clamping conditions can address this localized distortion mismatch. Overall, the laser welding model accurately reflected the behavior of the physical coupon post laser welding.

Hydroforming Model Results and Comparison

Hydroforming started with the prior residual stresses and strains from the welding model. In Fig. 12, a graph of the clamping force and internal pressure evolution is shown along with the Z displacement evolution at key points in time. At time point A in Fig. 12, the clamp was open and the distorted laser-welded blank was between the die and the table. From A to B, the clamp force was linearly increased until the closed condition was reached, resulting in the straightening of the welded bank as observed in the Z displacement, which returned to zero (green color). From B to C, the gas pressure on the internal faces of the blank was increased linearly, resulting in the yielding of the sheet against the die profile and formation of the channel (red). This continued from C to D as the pressure was constant for 0.5 s. From D to E, the internal gas pressure was then released linearly while the clamp force remained active. The clamp was removed at point F, and the inflated coupon could spring back.

The inflation model and the physical coupons exhibited the same distortion trends. The bow along the long axis of the coupon was predicted and correctly oriented toward the coupon’s laser-welded/channel side. The channel height spring back after inflation was also correctly predicted, with

a channel height approximately 1.32–1.75 mm tall compared to that previously measured for the physical coupon at 1.52–1.85 mm.

The surface deviation between the welding simulation and 3D scan data after best fit is shown in Fig. 13 for both C, the inflated laser/channel side, and D, the interface rim/flat side. The surface deviation between the simulation and the 3D light scan was within ± 0.5 mm on either side of the plate. Overall, the simulated coupons incorporating distortions from welding and gas inflation were in very good agreement, particularly regarding the bowing, channel heights, and global distortions.

Conclusions

A combined experimental and computational study of laser-welded and gas hydroforming/inflated aluminum alloy cold plates was developed and applied to an AA3105-H24 prototype coupon. Suitable laser parameters were determined for welding AA3105 1 mm to 1 mm aluminum sheet that could achieve hermetic sealing of the cold plate coupons. A coupled thermomechanical FE model was used to predict the coupon's temperature and strain field evolution during welding. The spring back was then compared to 3D scans of the physical coupon. Using the laser welding results, an FE model was then developed to simulate the inflation process where 500 lb/in.² gas was injected into the prewelded blank to deform and inflate the cold plate channels. The numerical methods developed here can be further applied to investigate more-complex cooling plate configurations where part quality (e.g., spring back) will be paramount to enable good interfacing with battery cells. The following major conclusions can be made:

1. The proposed combination of laser welding and gas inflation can form battery cold plates with nominally flat back sides for proper interfacing with battery cells, which helps minimize TIM thickness variation. The developed FE simulation accurately predicted the inflated cold plate coupon, exhibiting trends such as bowing along the long edge towards the laser welded side, post laser welding and post inflation, channel height spring back after inflation, and overall global distortion of the part.

2. The manufacturing simulation accurately predicted the global surface deviations between simulation and 3D light scans within ± 1.0 mm postwelding and ± 0.5 mm postinflation. However, the simulation did not accurately capture localized distortion around the interface rim postwelding. Lack of material data for the interface rim and heat input for the laser weld were likely key contributors.

3. Global distortion of the coupon decreased from the laser welding step at 1.88–3.74 mm in the physical scans to the inflation processing step at 1.57–1.80 mm. The FE model accurately predicted this, going from 2.25–2.33 mm post laser welding to 1.79–1.99 mm post inflation.

4. The channel height was found to spring back after inflation from a nominal 2 mm height as machined into the die to approximately 1.52–1.85 mm tall. The developed model accurately predicted a final channel height of approximately 1.32–1.75 mm. Accurate prediction of the channel geometry

is critical for the thermal performance of the cold panel, including fluid dynamic targets such as pressure drop and fluid velocity.

Statements and Declaration

All authors contributed to the writing of the manuscript. A.B. led project planning and 3D light scanning and assisted in FEA modeling. M.P. led laser weld characterization. N.A. led the FEA analysis. F.O. led software supervision. J.D. led laser welding studies and prototyping.

Conflict of Interest

The authors declare no competing interests. The authors did not receive financial support from any organization for the submitted work.

References

1. Wu, W., Wang, S., Wu, W., Chen, K., Hong, S., and Lai, Y. 2019. A critical review of battery thermal performance and liquid based battery thermal management. *Energy Conversion and Management* 182: 262–281. DOI: 10.1016/j.enconman.2018.12.051
2. Stadler, R., and Maurer, A. 2019. Methods for durability testing and lifetime estimation of thermal interface materials in batteries. *Batteries* 5(1): 34. DOI: 10.3390/batteries5010034
3. Zhao, H., and Woods, R. 2013. "Controlled atmosphere brazing of aluminum." In *Advances in Brazing*, edited by D. Sekulic., 280–322, 323e. Elsevier. DOI: 10.1533/9780857096500.2.280
4. Chu, E., and Xu, Y. 2004. Hydroforming of aluminum extrusion tubes for automotive applications. Part I: Buckling, wrinkling and bursting analyses of aluminum tubes. *International Journal of Medical Sciences* 46(2): 263–283. DOI: 10.1016/j.ijmecsci.2004.02.014
5. Möller, M., Haug, P., Scheible, P., Buse, C., Frischkorn, C., and Speker, N. 2022. Spatially tailored laser energy distribution using innovative optics for gas-tight welding of casted and wrought aluminum alloys in e-mobility. *Journal of Laser Applications* 34(4). DOI: 10.2351/7.0000735
6. Aminzadeh, A., Barka, N., El Ouafi, A., Mirakhorli, F., and Nadeau, F. 2024. Experimental analysis of overlap fiber laser welding for aluminum alloys: Porosity recognition and quality inspection. *Optics and Lasers in Engineering* 173(2): 107890. DOI: 10.1016/j.optlas-eng.2023.107890
7. Tao, W., and Yang, S. 2020. Weld zone porosity elimination process in remote laser welding of AA5182-O aluminum alloy lap-joints. *Journal of Materials Processing Technology* 286: 116826. DOI: 10.1016/j.jmatprotec.2020.116826
8. Lin, R., Wang, H., Lu, F., Solomon, J., and Carlson, B. E. 2017. Numerical study of keyhole dynamics and keyhole-induced porosity formation in remote laser welding of Al alloys. *Int. J. Heat Mass Transf.* 108: 244–256. DOI: 10.1016/j.ijheatmasstransfer.2016.12.019.
9. Cai, W., Saez, M., Spicer, P., Chakraborty, D., Skurkis, R., Carlson, B., Okigami, F., and Robertson, J. 2022. Distortion simulation of gas metal arc welding (GMAW) processes for automotive body assembly. *Welding in the World* 67: 109–139. DOI: 10.1007/s40194-022-01369-3
10. Derakhshan, E. D., Yazdian, N., Craft, B., Smith, S., and Kovacevic, R. 2018. Numerical simulation and experimental validation of residual stress and welding distortion induced by laser-based welding processes of thin structural steel plates in butt joint configuration. *Opt. Laser Technol.* 104: 170–182. DOI: 10.1016/j.optlastec.2018.02.026

11. Aminzadeh, A., Sattarpanah Karganroudi, S., Barka, N., and El Ouafi, A. 2021. A real-time 3D scanning of aluminum 5052-H32 laser welded blanks; geometrical and welding characterization. *Material Letters* 296(8): 129883. DOI:10.1016/j.matlet.2021.129883
12. Liu, X., Xu, Y. C., and Yuan, S. J. 2011. Hydro-forming of aluminum alloy complex-shaped components. *Transactions of Nonferrous Metals Society of China* (English Ed.). 21: s417to s422. DOI: org/10.1016/S1003-6326(11)61617-8
13. Lei, Q., Li, M., Ilinich, A., Luckey, G., and Misra, A. 2019 Micro-structural evolution and failure mechanism of an extrusion welded aluminum alloy tube during hydroforming processing. *Materials Science and Engineering: A* 756: 346–353. DOI: 10.1016/j.msea.2019.03.066
14. Lang, L, Yuan, S., Wang, X., Wang, Z. R., Fu, Z., Danckert, J., and Nielsen, K. B. 2004. A study on numerical simulation of hydroforming of aluminum alloy tube. *J. Mater. Process. Technol.* 146(3): 377–388. DOI: 10.1016/j.jmatprotec.2003.11.031
15. Li, K., Lu, F., Guo, S., Cui, H., and Tang, X. 2015. Porosity sensitivity of A356 Al alloy during fiber laser welding. *Trans. Nonferrous Met. Soc. China* 25 (8) 2516–2523. DOI: 10.1016/S1003-6326(15)63870-5
16. Wang, L., Yao, M., Gao, X., Kong, F., Tang, J., and Jun Kim, M. 2023 Keyhole stability and surface quality during novel adjustable-ring mode laser (ARM) welding of aluminum alloy. *Optics & Laser Technology* 161: 09202. DOI: 10.1016/j.optlastec.2023.109202
17. Mohammadpour, M., Wang, L., Kong, F., and Kovacevic, R. 2020. Adjustable ring mode and single beam fiber lasers: A performance comparison. *Manufacturing Letters* 25(8): 50–55. DOI: 10.1016/j.mfglet.2020.07.003
18. Fetzer, F., Sommer, M., Weber, R., Weberpals, J. P., and Graf, T. 2018. Reduction of pores by means of laser beam oscillation during remote welding of AlMgSi. *Optics and Lasers in Engineering* 108(9): 68–77. DOI: 10.1016/j.optlaseng.2018.04.012
19. Li, S., Mi, G., and Wang, C. 2020. A study on laser beam oscillating welding characteristics for the 5083 aluminum alloy: Morphology, microstructure and mechanical properties. *J. Manuf. Process.* 53(5): 12–20. DOI: 10.1016/j.jmapro.2020.01.018
20. Ke, W., Bu, X., Oliveira, J. P., Xu, W. G., Wang, Z., and Zeng, Z. 2021. Modeling and numerical study of keyhole-induced porosity formation in laser beam oscillating welding of 5A06 aluminum alloy. *Optics & Laser Technology* 133(1): 106540. DOI: 10.1016/j.optlastec.2020.106540
21. Huang, S., Lu, R., Lou, M., Lv, T., Yao, J. and Li, Y. 2024. Effect of oscillation parameters on adjustable-ring mode (ARM) laser beam welding of aluminum alloys. *Journal of Manuf. Process.* 113: 307–318. DOI: 10.1016/j.jmapro.2024.01.060
22. Allu, P. 2019. 2019. CFD simulations for laser welding of Al alloys. *Lasers in Manuf. Conf. 2019*, 1–6.
23. Moraitis, G. A., and Labeas, G. N. 2008. Residual stress and distortion calculation of laser beam welding for aluminum lap joints. *J. Mater. Process. Technol.* 198(1–3): 260–269. DOI: 10.1016/j.jmatprotec.2007.07.013
24. Chen, X., Tang, S., Xie, W., and Zhang, D. 2024 Numerical Simulation Study of Laser-arc Hybrid Welding of 6063/5083 Aluminum Alloy. *J. Mater. Eng. Perform.* DOI: 10.1007/s11665-024-09842-4
25. Ahmetoglu, M., Sutter, K., Li, X. J., and Altan, T. 2000. Tube hydroforming: Current research, applications and need for training. *J. Mater. Process. Technol.* 98(2): 224–231. DOI: 10.1016/S0924-0136(99)00203-4
26. Grizelj, B., Cumin, J., and Ergić, T. 2009. Application of hydro-forming process in sheet metal formation. *Strojarstvo* 51: 333–340.
27. Abedrabbo, N., Zampaloni, M. A., and Pourboghrat, F. 2005. Wrinkling control in aluminum sheet hydroforming. *Int. J. Mech. Sci.* 47(3): 333–358. DOI: 10.1016/j.ijmecsci.2005.02.003
28. Karabegović, E., and Poljak, J. 2016. Experimental modeling of fluid pressure during hydroforming of welded plates. *Adv. Prod. Eng. Manag.* 11: 345–354. DOI: 10.14743/apem2016.4.232
29. Wang, L., Mohammadpour, M., Yang, B., Gao, X., Lavoie, J.-P., Kleine, K., Kong, F., and Kovacevic, R. 2020. Monitoring of keyhole entrance and molten pool with quality analysis during adjustable ring mode laser welding. *Applied Optics* 59(6): 1576. DOI: 10.1364/AO.383232
30. *Simufact Welding Theoretical Background Manual*. 2018.

ANDREW BOBEL (andrew.bobel@gm.com) and **MASOUD POUR** are with General Motors Global R&D Center, Warren, Mich. **NICHOLAS AVEDISSIAN** and **FERNANDO OKIGAMI** are with Hexagon Manufacturing Intelligence, North Kingstown, R.I. **JON DELBOY** is with KUKA Systems North America, Sterling Heights, Mich.